Elsevier Editorial System(tm) for Control Engineering Practice
Manuscript Draft

Manuscript Number:

Title: Nonlinear Region of Attraction Analysis for Flight Control Verification and Validation

Article Type: Regular article

Keywords: Validation and Verification; Region of Attraction;
Nonlinear Analysis; Flight Control

Corresponding Author: Mr. Abhijit Chakraborty,

Corresponding Author's Institution: University of Minnesota

First Author: Abhijit Chakraborty

Order of Authors: Abhijit Chakraborty; Peter Seiler; Gary J Balas

Abstract: Current practice for flight control validation relies heavily on linear analyses and nonlinear, high-fidelity simulations. This process would be enhanced by the addition of nonlinear analyses of the flight control system. This paper demonstrates the use of region of attraction estimation for studying nonlinear effects. A nonlinear polynomial model is constructed for the longitudinal dynamics of NASA's Generic Transport Model aircraft. A polynomial model for the short period dynamics is obtained by decoupling this mode from the nonlinear longitudinal model. Polynomial optimization techniques are applied to estimate region of attractions around trim conditions.

CONTROL ENGINEERING PRACTICE

PAPER CHECKLIST for the preparation of papers.

Please ensure that your paper conforms to the following guidelines.

1 PREFERRED FORMAT AND LAYOUT:

- ❑ **Title**: Less than 10 words
- ❑ Running headline provided
- ❑ **Authors' names**
- ❑ **Authors' affiliations/addresses**
- ❑ **Address** including fax number and email address **of corresponding author**
- ❑ **Abstract**: max. 100 words
- ❑ **Keywords**: 5–10
- ❑ **Font:** Times Roman/Times New Roman (all text, including headings and figure legends)
- ❑ **Single-column printout**
- ❑ **Double-spaced text**
- ❑ **Main headings**: Upper and lower case
- ❑ Numbered (1, 2, etc.)
- ❑ **Secondary headings**: Upper and lower case
- ❑ Numbered (1.1, 1.2, etc.)
- ❑ **Tertiary headings**: Upper and lower case
- ❑ Not numbered
- ❑ **Figures**: Acceptable line quality
- ❑ Legible text (spellings, etc., checked)
- ❑ Provided within the text
- ❑ **Figure legends**: Separate list provided
- ❑ **Tables**: No vertical lines
- ❑ Provided within the text
- ❑ **References**: Harvard style
- ❑ Correct usage within the text
- ❑ **All** references cited in the text
- ❑ **All** cited references listed
- ❑ **Matrices**: boldface upper case
- ❑ **Vectors**: boldface lower case
- ❑ **Other variables**: Italics
- ❑ **Units**: SI
- ❑ **Language**: Spelling checked
- ❑ Grammar checked
- ❑ **Use of first person ("I/we", etc.) strictly eliminated**

2. REFEREES' SPECIFIC REQUESTS

Provided on separate sheets, if available.

Nonlinear Region of Attraction Analysis for Flight Control Verification and Validation

Abhijit Chakraborty[a,1,*], Peter Seiler[a], Gary J. Balas[a]

[a] *Aerospace Engineering & Mechanics, University of Minnesota, Minneapolis, MN 55454*

Abstract

Current practice for flight control validation relies heavily on linear analyses and nonlinear, high-fidelity simulations. This process would be enhanced by the addition of nonlinear analyses of the flight control system. This paper demonstrates the use of region of attraction estimation for studying nonlinear effects. A nonlinear polynomial model is constructed for the longitudinal dynamics of NASA's Generic Transport Model aircraft. A polynomial model for the short period dynamics is obtained by decoupling this mode from the nonlinear longitudinal model. Polynomial optimization techniques are applied to estimate region of attractions around trim conditions.

Keywords: Validation and Verification, Region of Attraction, Nonlinear Analysis, Flight Control

1. Introduction

Safety critical flight systems require extensive validation prior to entry into service. Validation of the flight control system is becoming more dif-

*Corresponding author
Email addresses: chakrab@aem.umn.edu (Abhijit Chakraborty), seiler@aem.umn.edu (Peter Seiler), balas@aem.umn.edu (Gary J. Balas)
[1]107 Akerman Hall, 110 Union St. SE, Minneapolis, MN 55454, (1) 612-625-6561

ficult due to the increased use of advanced flight control algorithms, e.g. adaptive flight controls. NASA's Aviation Safety Program (AvSP) aims to reduce the fatal (commercial) aircraft accident rate by 90% by 2022 (Heller et al., 2003). A key challenge in achieving this goal is the need for extensive validation and certification tools for the flight systems. The current certification and validation procedure involves analytical, simulation-based and experimental techniques (Heller et al., 2003). Current practice is to assess the closed-loop stability and performance characteristics of the aircraft flight control system around numerous trim conditions using linear analysis tools. The linear analysis methods include stability margins, robustness analysis and worst-case analysis. The linear analysis results are supplemented with Monte Carlo simulations of the full nonlinear equations of motion to provide further confidence in the system performance and to uncover nonlinear dynamic characteristics, e.g. limit cycles, that are not revealed by the linear analyses. To summarize, current practice involves extensive linear analysis at different trim conditions and probabilistic nonlinear simulation results. The certification process typically does not involve any analytical nonlinear methods.

The gap between linear analyses and Monte Carlo simulations can cause significant nonlinear effects to go undetected. For example, several F/A-18 aircraft were lost due to a nonlinear loss-of-control phenomenon known as the falling leaf mode (Jaramillo and Ralston, 1996; Heller et al., 1999; Lluch, 1998; Heller et al., 2004). Linear analysis tools did not detect the potential of the closed-loop system to exhibit the falling leaf mode. Thus there is a need for nonlinear analysis tools to fill this gap (Chakraborty et al., 2009).

Recently, significant research has been performed on the development of nonlinear analysis tools for computing regions of attraction, reachability sets, input-output gains, and robustness with respect to uncertainty for nonlinear polynomial systems (Tan, 2006; Tan et al., 2008; Topcu et al., 2007, 2008; Chiang and Thorp, 1989; Davison and Kurak, 1971; Genesio et al., 1985; Tibken, 2000; Tibken and Fan, 2006; Vannelli and Vidyasagar, 1985; Parrilo, 2000). These tools make use of polynomial sum-of-squares optimization (Parrilo, 2000). These tools can only be applied to the dynamics described by polynomial vector field . These techniques offer great potential to bridge the gap in the flight control validation process.

The objective of this paper is to demonstrate the advantage of including nonlinear analysis tools based on SOS techniques in the flight control law validation process. The computational requirements for sum-of-squares (SOS) optimizations grow rapidly in the number of variables and polynomial degree. This roughly limits SOS methods to nonlinear analysis problems with at most 8-10 states and degree 3-5 polynomial models. Consequently, the construction of accurate, low-degree polynomial models is an important step in the proposed analysis process.

This paper applies the nonlinear analysis tools on NASA's Generic Transport Model (GTM) aircraft (Cox, 2009; Murch and Foster, 2007). The GTM is the primary test aircraft for NASA's Airborne Subscale Transport Aircraft Research (AirSTAR) flight test facility (Jordan and Bailey, 2008; Jordan et al., 2006; Bailey et al., 2005). The AirSTAR program addresses the challenges associated with validating flight control law in adverse condition (Murch et al., 2009; Murch, 2008; Gregory et al., 2009). The polynomial

model constructed in this paper accurately represents the longitudinal dynamics of NASA's Generic Transport Model (GTM) aircraft and it is suitable to address the issues with flight control law validation and verification.

The paper has the following structure. First, a polynomial model of the longitudinal dynamics of NASA's GTM aircraft (Cox, 2009; Murch and Foster, 2007) is constructed in Section 2. The longitudinal dynamics consist of a phugoid and short period mode. In Section 2.3, a polynomial model for the short period dynamics is obtained by decoupling this mode from the nonlinear longitudinal model. This nonlinear short period model is of interest because the decoupling of the longitudinal modes is typically done using linearized models. Section 3 describes a computational procedure to estimate regions of attraction for polynomial systems (Jarvis-Wloszek, 2003; Jarvis-Wloszek et al., 2003; Tan and Packard, 2004; Jarvis-Wloszek et al., 2005; Tan, 2006; Topcu et al., 2007, 2008). This algorithm is applied in Section 4 to estimate regions of attractions for the open-loop short period dynamics and a closed-loop longitudinal GTM aircraft. The analysis of the two-state short period model in Section 4 is for illustrative purposes since the system trajectories can be entirely visualized in a phase-plane diagram. This model is used to demonstrate that the linearized model fails to capture significant nonlinear effects. The analysis of the four-state longitudinal GTM aircraft demonstrates that the nonlinear region-of-attraction (ROA) computational procedure can be applied to systems with higher state dimensions. The paper concludes with a summary of the contribution of the paper.

2. Polynomial Aircraft Models

NASA's Generic Transport Model (GTM) describes a remote-controlled 5.5 percent scale commercial aircraft (Cox, 2009; Murch and Foster, 2007). The main GTM aircraft parameters are provided in Table 1. NASA constructed a high fidelity 6 degree-of-freedom Simulink model of the GTM with the aerodynamic coefficients described as look-up tables. This section describes the construction of polynomial models of the GTM longitudinal and short period dynamics based on the look-up table data.

Table 1: Aircraft and Environment Parameters

Wing Area, S	0.5483 m^2
Mean Aerodynamic Chord, $\bar{c}$	0.2790 m
Mass, m	22.50 kg
Pitch Axis Moment of Inertia, I_{yy}	5.768 kg-m^2
Air Density, ρ	1.224 kg/m^3
Gravity Constant, g	9.810 m/s^2

2.1. Longitudinal Dynamics

The longitudinal dynamics of the GTM are described by a standard four-state longitudinal model (Stevens and Lewis, 1992):

$$\dot{V} = \frac{1}{m}\left(-D - mg\sin\left(\theta - \alpha\right) + T_x\cos\alpha + T_z\sin\alpha\right) \tag{1}$$

$$\dot{\alpha} = \frac{1}{mV}\left(-L + mg\cos\left(\theta - \alpha\right) - T_x\sin\alpha + T_z\cos\alpha\right) + q \tag{2}$$

$$\dot{q} = \frac{\left(M + T_m\right)}{I_{yy}} \tag{3}$$

$$\dot{\theta} = q \tag{4}$$

where V is the air speed (m/s), α is the angle of attack (rad), q is the pitch rate (rad/s) and θ is the pitch angle (rad). The control inputs are the elevator deflection δ_{elev} (rad) and engine throttle δ_{th} (percent). For ease of interpretation, plots of α, q and δ_{elev} are shown in units of degs, degs/s, and degs, respectively.

The drag force D (N), lift force L (N), and aerodynamic pitching moment M (N-m) are given by:

$$D = \bar{q}SC_D(\alpha, \delta_{elev}, \hat{q}) \tag{5}$$

$$L = \bar{q}SC_L(\alpha, \delta_{elev}, \hat{q}) \tag{6}$$

$$M = \bar{q}S\bar{c}C_m(\alpha, \delta_{elev}, \hat{q}) \tag{7}$$

where $\bar{q} := \frac{1}{2}\rho V^2$ is the dynamic pressure (N/m^2) and $\hat{q} := \frac{\bar{c}}{2V}q$ is the normalized pitch rate (unitless). C_D, C_L, and C_m are unitless aerodynamic coefficients computed from look-up tables provided by NASA.

The GTM has one engine on the port side and one on the starboard side of the airframe. Equal thrust settings for both engines is assumed. The thrust from a single engine T (N) is a function of the throttle setting δ_{th} (percent). $T(\delta_{th})$ is a given ninth-order polynomial in NASA's high fidelity GTM simulation model. T_x (N) and T_z (N) denote the projection of the total engine thrust along the body x-axis and body-z axis, respectively. T_m (N-m) denotes the pitching moment due to both engines. T_x, T_z and T_m are given by:

$$T_x(\delta_{th}) = n_{ENG}T(\delta_{th})\cos(\epsilon_2)\cos(\epsilon_3) \tag{8}$$

$$T_z(\delta_{th}) = n_{ENG}T(\delta_{th})\sin(\epsilon_2)\cos(\epsilon_3) \tag{9}$$

$$T_m(\delta_{th}) = r_z T_x(\delta_{th}) - r_x T_z(\delta_{th}) \tag{10}$$

$n_{ENG} = 2$ is the number of engines. $\epsilon_2 = 0.0375$ rad and $\epsilon_3 = -0.0294$ rad are angles that specify the rotation from engine axes to the airplane body axes. $r_x = 0.1371$ m and $r_z = 0.0907$ m specify the moment arm of the thrust.

2.2. Polynomial Longitudinal Model

The following terms of the longitudinal model presented in Section 2.1 are approximated by low-order polynomials:

1. Trigonometric functions: $\sin(\alpha)$, $\cos(\alpha)$, $\sin(\theta - \alpha)$, $\cos(\theta - \alpha)$
2. Engine model: $T(\delta_{th})$
3. Rational dependence on speed: $\dfrac{1}{V}$
4. Aerodynamic coefficients: C_D, C_L, C_m

Constructing polynomial approximations for the trigonometric functions, engine model, and rational dependence on speed is relatively straight-forward. The trigonometric functions are approximated by Taylor series expansions: $\sin z \approx z - \frac{1}{6}z^3$ and $\cos z \approx 1 - \frac{1}{2}z^2$ for z in units of radians. For $|z| \leq \frac{\pi}{4}$ rad the maximum approximation error for the sine and cosine functions is 0.35% and 2.2%, respectively. For the engine model, a least squares technique is used to approximate the ninth order polynomial function $T(\delta_{th})$ by the following third order polynomial:

$$T(\delta_{th}) \approx -8.751 \times 10^{-6}\delta_{th}^3 + 5.115 \times 10^{-3}\delta_{th}^2 + 3.673 \times 10^{-1}\delta_{th} + 4.825 \quad (11)$$

The maximum approximation error is 1.3% over the full range throttle inputs $\delta_{th} \in [0\%, 100\%]$. The least squares technique is also used to compute a linear

fit to $\frac{1}{V}$ over the desired range of interest from 30 m/s to 60 m/s:

$$\frac{1}{V} \approx -5.304 \times 10^{-4} V + 4.699 \times 10^{-2} \tag{12}$$

The maximum approximation error is 9% over the specified velocity range. The linear fit for $\frac{1}{V}$ is used in both the $\dot{\alpha}$ equation and the equation for the normalized pitch rate $\hat{q}$.

Derivation of the polynomial approximations for the aerodynamic coefficients requires a more detailed explanation. NASA provides raw look-up table data for the aerodynamic coefficients in the airframe body axes, i.e. the raw data is provided for C_X, C_Z, and C_m.[2] In addition, each aerodynamic coefficient is computed as a sum of three terms which model the aerodynamic effects of the basic airframe, elevator inputs, and pitch rate. For example, $C_X(\alpha, \delta_{elev}, \hat{q})$ is a sum of three terms each of which is computed from a look-up table:

$$C_X(\alpha, \delta_{elev}, \hat{q}) = C_{X,\alpha}(\alpha) + C_{X,\delta_{elev}}(\alpha, \delta_{elev}) + C_{X,\hat{q}}(\alpha, \hat{q}) \tag{13}$$

$C_{X,\alpha}$ models the basic airframe dependence of the body-X force on the angle of attack. $C_{X,\delta_{elev}}$ and $C_{X,\hat{q}}$ model the aerodynamic effects of the elevator input and pitch rate, respectively. All body-axis look-up tables were transformed into lift and drag coordinates via a rotation:

$$\begin{bmatrix} C_D \\ C_L \end{bmatrix} = - \begin{bmatrix} \cos(\alpha) & \sin(\alpha) \\ -\sin(\alpha) & \cos(\alpha) \end{bmatrix} \begin{bmatrix} C_X \\ C_Z \end{bmatrix} \tag{14}$$

[2]The notation refers to standard aircraft body axis conventions (Stevens and Lewis, 1992). x is directed to the front along the longitudinal axis of the aircraft and z is directed down. X and Z are the aerodynamic forces along the x and z axes, respectively.

A weighted least squares technique is used to fit the lift and drag look-up table data. Accurate, low-order polynomial fits could be obtained for all look-up tables after rotating into the lift and drag coordinates. For example, Figures 1, 2 and 3 show the look-up table data and cubic polynomial fits for $C_{L,\alpha}$, $C_{D,\alpha}$ and $C_{m,\alpha}$. The polynomial function approximations for all aerodynamic coefficient look-up tables are provided in Appendix Appendix A.1.

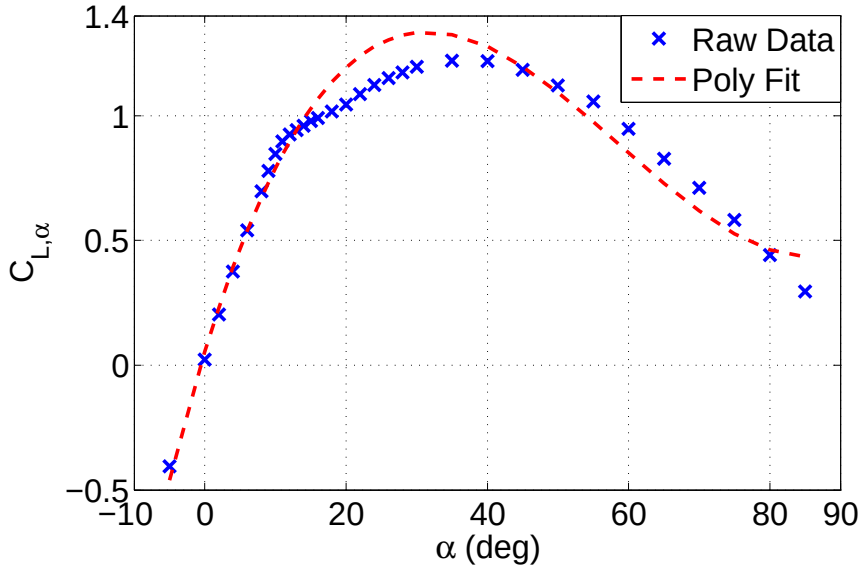

Figure 1: Look-up table data and polynomial fit for $C_{L,\alpha}$

There are two important issues in this fitting procedure. First, the fitting of the C_L/C_D data rather than the raw C_X/C_Y is justified by the structure of the dynamic equations. For example, $-D$ enters directly into the equation for $\dot{V}$ (Equation 1). $\dot{V}$ can be alternatively expressed in terms of X and Z forces via the substitution $-D = X\cos(\alpha) + Z\sin(\alpha)$. In this form fitting the raw

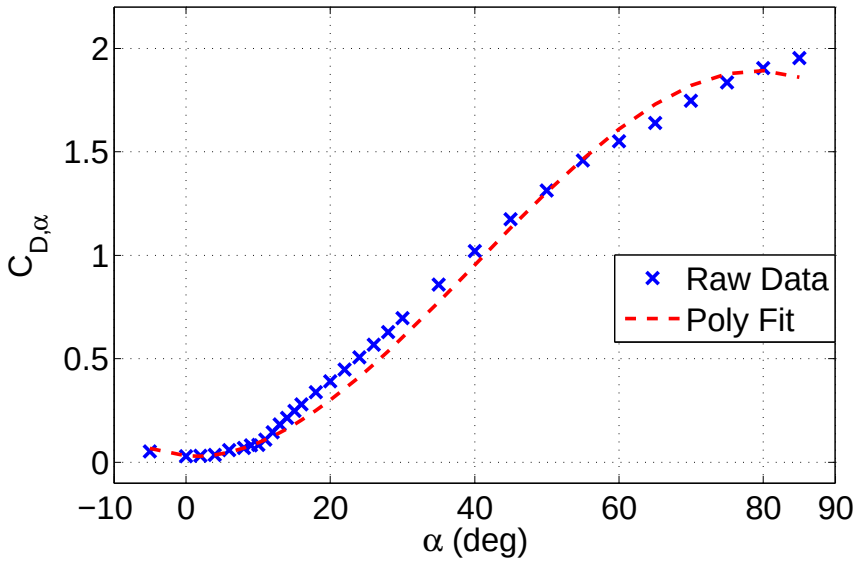

Figure 2: Look-up table data and polynomial fit for $C_{D,\alpha}$

aerodynamic look-up data for C_X and C_Z would introduce approximation errors in X and Z. Approximation errors would also be introduced by the polynomial fits for $\cos(\alpha)$ and $\sin(\alpha)$. Directly fitting the look-up data for C_D only leads to one lumped approximation error in the $-D$ term. Second, the least squares solutions for the lift/drag/pitching moment data were weighted to obtain extremely accurate fits at low angles of attack ($-5^o \leq \alpha \leq 15^o$) and less accurate fits at higher angles of attack ($\alpha \geq 15^o$). This weighting ensures that the polynomial model retains trim characteristics that are similar to those of the original nonlinear model. Note that the polynomial fits fail to capture important characteristics of the look-up table data of $C_{L,\alpha}$ and $C_{m,\alpha}$ for angles of attack between $15^o \leq \alpha \leq 40^o$. In fact, trimming both the models around $\alpha \approx 11$deg results unstable linearization for the original longi-

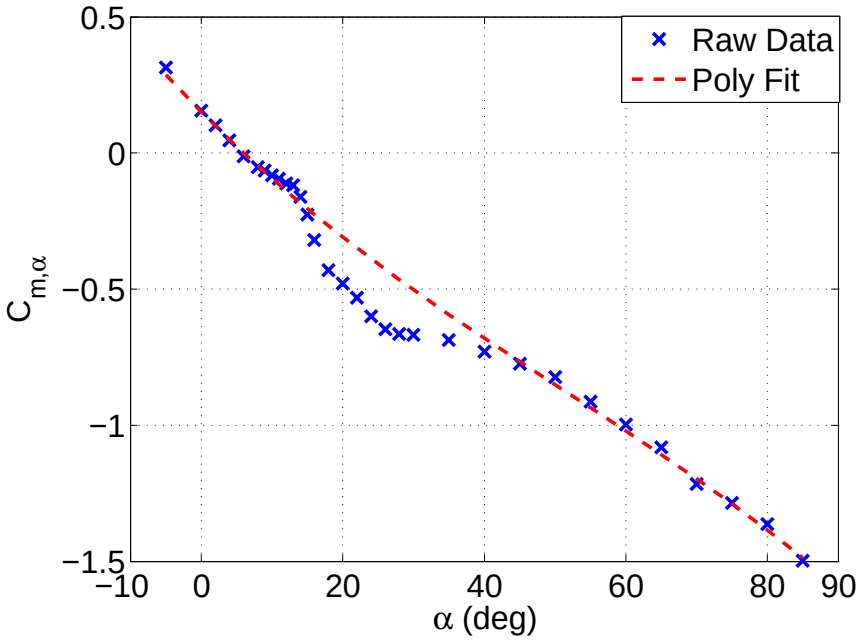

Figure 3: Look-up table data and polynomial fit for $C_{m,\alpha}$

tudinal model, and stable linearization for the polynomial model. However, the unstable pole in the original model is slow enough ($\approx 10^{-2}$ rad/s) not to affect the feedback characteristics for the polynomial model after closing the loop with the control law. Moreover, both the models were simulated with numerous doublet and step inputs. The qualitative characteristics of both the trajectories are similar, even when the linearizations are different. The original model has more damping than the polynomial model around $\alpha \approx 20$deg and this can be seen from Figure 3. The mismatch between the raw data and the polynomial fitting causes the polynomial and look-up table models to have different trim characteristics for angles of attack in this range. However, the analyses presented in this paper correspond to low angle

of attack ($\alpha \approx 2 - 3^o$) trim conditions.

A degree seven polynomial model is obtained after replacing all non-polynomial terms with their polynomial approximations. The polynomial model takes the form:

$$\dot{x} = f(x, u) \tag{15}$$

where $x := [V(\text{m/s}),\ \alpha(\text{rad}),\ q(\text{rad/s}),\ \theta(\text{rad})]$, and $u := [\delta_{elev}(\text{rad}),\ \delta_{th}(\%)]$. The degree seven polynomial model $f(x, u)$ is provided in Appendix Appendix A.2.

The trim conditions for level flight across the range of velocities $V \in [30, 60]$ m/s are computed to assess the quality of the polynomial approximation. The trim conditions assume level flight ($\alpha = \theta$) and no pitch rate ($q = 0$ deg/s). Figure 4 shows the trim angle-of-attack α and trim inputs ($\delta_{elev},\ \delta_{th}$) versus trim speed for both the original nonlinear model and the polynomial approximation. The trim behavior of the polynomial model is similar to the original nonlinear model. Both models were simulated with a variety of step and doublet inputs and the time-domain responses were similar.

The polynomial approximation to the original nonlinear model is only valid within a certain region of state-space. The polynomial approximation for the trigonometric function ($\sin(\alpha)$, $\cos(\alpha)$ etc.) is valid up to approximately ± 50 deg for the corresponding angle. This provides an upper bound on the range of validity for the polynomial model in the α direction. The look-up table data for the basic airframe aerodynamic coefficients is within the range of 5 deg $\leq \alpha \leq$ 85 deg, providing a lower bound on the region of validity in α direction. Hence, the polynomial model is valid for

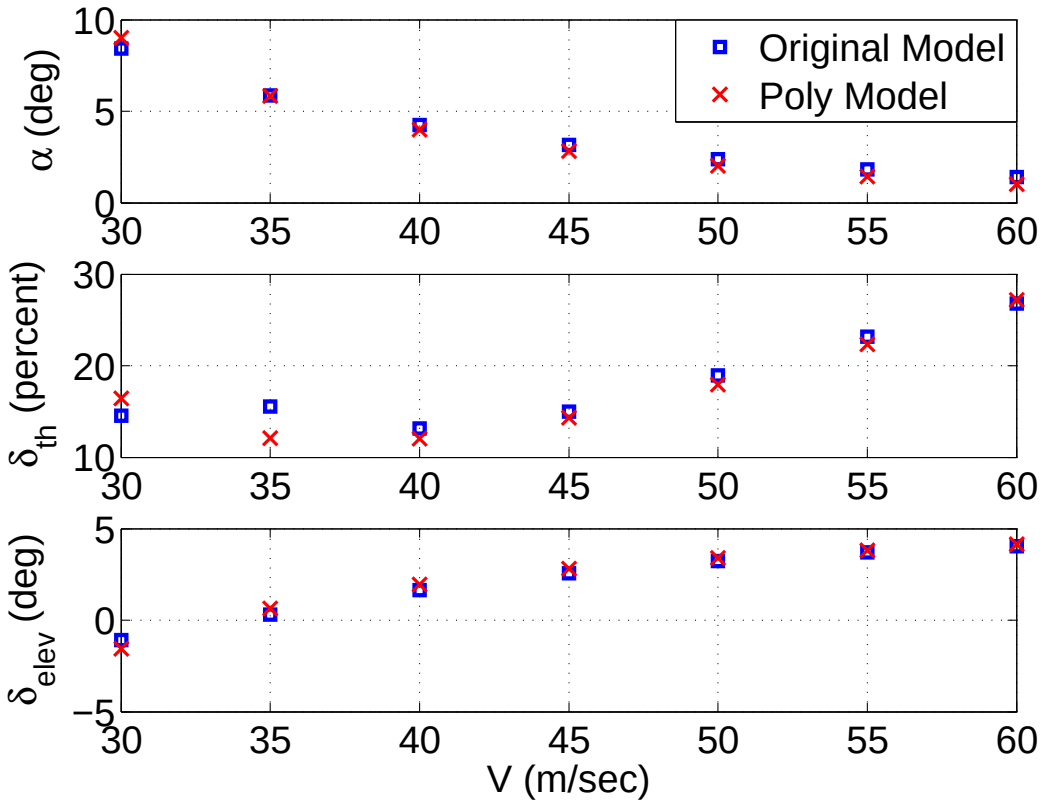

Figure 4: Trim angle of attack and inputs vs. trim speed

5 deg $\leq \alpha \leq$ 50 deg. The least-square approximation to the rational dependence on speed $(\frac{1}{V})$ is valid over the range from 30 m/s to 60 m/s with a maximum error of approximately 9%. The least-square approximation of the look-up table data to the rate derivative terms, i.e. $C_{L,\hat{q}}$, $C_{D,\hat{q}}$, $C_{m,\hat{q}}$, is valid for -70 deg/s $\leq q \leq$ 70 deg/s. This limits the range of validity in the pitch rate direction. The polynomial model is valid within the above specified region in the state-space.

This validation procedure is heuristic but it is still an open problem to develop rigorous and computable metrics of the approximation error between a generic nonlinear (non-analytic) model and a polynomial model. There are many ways to conceptually extend linear system metrics, e.g. the H_∞ norm, but the difficulty is in obtaining algorithms to easily compute these metrics for nontrivial nonlinear systems.

2.3. Polynomial Short Period Model

The longitudinal dynamics of an aircraft consist of a phugoid and short period mode. The phugoid mode is a long duration oscillation involving air speed and pitch angle. The short period mode is a faster oscillation involving angle-of-attack and pitch rate. The 4-state model of the longitudinal aircraft dynamics (Equations 1-4) can be decoupled into models of the short period (α and q) and phugoid (V and θ) modes. This decoupling is typically done on the linearized model of the longitudinal dynamics (Stevens and Lewis, 1992). In fact, this decoupling can be done, to a good approximation, on the nonlinear longitudinal dynamics. The resulting nonlinear short period model provides a simpler model for nonlinear analysis than the 4-state longitudinal model. This nonlinear short period model is of interest to flight control engineers since the short period mode is an important determinant of the aircraft flying and handling qualities. Moreover, the decoupled nonlinear short period model may provide insight for the design an inner-loop control laws in presence of the nonlinearities. The remainder of this section describes the construction of the nonlinear short period model.

Consider the flight condition at level flight and the speed $V = 45$ m/s:

$$\begin{bmatrix} V_t \\ \alpha_t \\ q_t \\ \theta_t \end{bmatrix} = \begin{bmatrix} 45.00 \text{ m/s} \\ 0.04924 \text{ rad} \\ 0 \text{ rad/s}, \\ 0.04924 \text{ rad} \end{bmatrix}, \quad \begin{bmatrix} \delta_{elev,t} \\ \delta_{th,t} \end{bmatrix} = \begin{bmatrix} 14.33 \ \% \\ 0.04892 \text{ rad} \end{bmatrix} \tag{16}$$

The subscript "t" denotes a trim value. A polynomial short period model is extracted from the 4-state polynomial model, Equation (15), by holding V, θ and δ_{th} at their trim values. Define two polynomials:

$$g_1(\alpha, q, \delta_{elev}) := f_2(x, u)\big|_{(x,u)=\left([V_t,\alpha,q,\theta_t],[\delta_{th,t},\delta_{elev}]\right)} \tag{17}$$

$$g_2(\alpha, q, \delta_{elev}) := f_3(x, u)\big|_{(x,u)=\left([V_t,\alpha,q,\theta_t],[\delta_{th,t},\delta_{elev}]\right)} \tag{18}$$

where f_2 and f_3 are from the 4-state polynomial longitudinal model provided in Appendix Appendix A.2. The polynomial short period is given by:

$$\dot{\alpha} = g_1(\alpha, q, \delta_{elev}) \tag{19}$$

$$\dot{q} = g_2(\alpha, q, \delta_{elev}) \tag{20}$$

The short period model has two states $[\alpha,\ q]^T$ and one input δ_{elev}.

A simulation comparison is performed to verify that the polynomial short period model provides a good approximation for the short period mode of the original 4-state longitudinal model (Equations 1-4). The short period model is simulated from many initial conditions $[\alpha(0), q(0)]$ with the elevator held fixed at the trim value. The original 4-state model is also simulated starting from initial conditions of the form $[V_t, \alpha(0), q(0), \theta_t]$ with both inputs held fixed at their trim values. In Figure 5, the phase plane for the short period model is shown in solid paths while the projection of the four-state simulation

trajectory onto the (α, q) plane is shown in dotted paths. This phase plane comparison shows that there is excellent agreement between the trajectories of the two models over a wide range of initial conditions. The main differences occur as the trajectories converge to the trim point. This is due to the short period model converging to the trim condition while the phugoid mode in the 4-state longitudinal model causes the trajectories to have a slow, low-amplitude oscillatory behavior near the trim point. In addition to this phase plane comparison, good agreement was observed between the two models for simulations with step and doublet inputs.

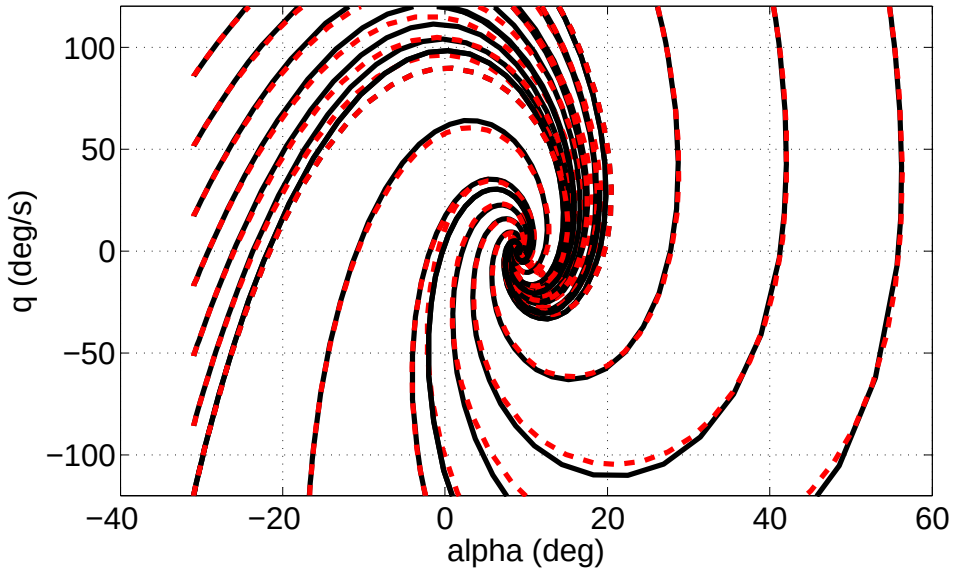

Figure 5: Phase Plane Comparison of Polynomial Short Period (Solid) and 4-state Polynomial Models (Dashed)

3. Region of Attraction Estimation

This section provides a brief overview of a computational method to estimate the region of attraction (ROA). Consider an autonomous nonlinear dynamical system of the form:

$$\dot{x} = f(x),\ x(0) = x_0 \tag{21}$$

where $x \in \mathbb{R}^n$ is the state vector and $f : \mathbb{R}^n \to \mathbb{R}^n$ is a multivariable polynomial. Assume that $x = 0$ is a locally asymptotically stable equilibrium point. Formally, the ROA is defined as:

$$\mathcal{R} = \left\{ x_0 \in \mathbb{R}^n :\ \text{If } x(0) = x_0 \text{ then } \lim_{t\to\infty} x(t) = 0 \right\} \tag{22}$$

Computing the exact ROA for nonlinear dynamical systems is very difficult. There has been significant research devoted to estimating invariant subsets of the ROA (Parrilo, 2000; Vannelli and Vidyasagar, 1985; Tibken and Fan, 2006; Tibken, 2000; Hauser and Lai, 1992; Hachicho and Tibken, 2002; Genesio et al., 1985; Davison and Kurak, 1971; Chiang and Thorp, 1989). The approach taken in this paper is to restrict the search to ellipsoidal approximations of the ROA. Given an $n \times n$ matrix $N = N^T > 0$, define the shape function $p(x) := x^T N x$ and level set $\mathcal{E}_\beta := \{x \in \mathbb{R}^n \ :\ p(x) \leq \beta\}$. $p(x)$ defines the shape of the ellipsoid and β determines the size of the ellipsoid $\mathcal{E}_\beta$. The choice of p is problem dependent and reflects dimensional scaling information as well as the importance of certain directions in the state space. Given the shape function p, the problem is to find the largest ellipsoid $\mathcal{E}_\beta$

contained in the ROA:

$$\beta^* = \max \beta \tag{23}$$
$$\text{subject to: } \mathcal{E}_\beta \subset \mathcal{R}$$

Determining the best ellipsoidal approximation to the ROA is still a challenging computational problem. Instead, lower and upper bounds for β^* satisfying $\underline{\beta} \leq \beta^* \leq \bar{\beta}$ are computed. If the lower and upper bounds are close then the largest ellipsoid level set, defined by Equation (23), has been approximately computed.

The upper bounds are computed via a search for initial conditions leading to divergent trajectories. If $\lim_{t\to\infty} x(t) = +\infty$ when starting from $x(0) = x_{0,div}$ then $x_{0,div} \notin \mathcal{R}$. If we define $\bar{\beta}_{div} := p(x_{0,div})$ then $\mathcal{E}_{\bar{\beta}_{div}} \not\subset \mathcal{R}$ which implies $\beta^* \leq \bar{\beta}_{div}$ and $\mathcal{E}_{\beta^*} \subseteq \mathcal{E}_{\bar{\beta}_{div}}$. An exhaustive Monte Carlo search is used to find the tightest possible upper bound on β^*. Specifically, random initial conditions are chosen starting on the boundary of a large ellipsoid: Choose x_0 satisfying $p(x_0) = \beta_{try}$ where β_{try} is sufficiently large that $\beta_{try} \gg \beta^*$. If a divergent trajectory is found, the initial condition is stored and an upper bound on β^* is computed. β_{try} is then decreased by a factor of 0.995 and the search continues until a maximum number of simulations is reached. $\bar{\beta}_{MC}$ will denote the smallest upper bound computed with this Monte Carlo search.

The lower bounds are computed using Lyapunov functions and recent results connecting sums-of-squares polynomials to semidefinite programming. Computing these bounds requires the vector field $f(x)$ in Equation (21) to be a polynomial function. The computational algorithm is briefly described here and full algorithmic details are provided elsewhere (Jarvis-Wloszek, 2003; Jarvis-Wloszek et al., 2003; Tan and Packard, 2004; Jarvis-Wloszek et al.,

2005; Tan, 2006; Topcu et al., 2007, 2008). Lemma 1 is the main Lyapunov theorem used to compute lower bounds on β^*. This specific lemma is proved by Tan (2006) but very similar results are given in textbooks, e.g. by Vidyasagar (1993).

Lemma 1. *If there exists $\gamma > 0$ and a polynomial $V : \mathbb{R}^n \to \mathbb{R}$ such that:*

$$V(0) = 0 \text{ and } V(x) > 0 \ \forall x \neq 0 \tag{24}$$

$$\Omega_\gamma := \{x \in \mathbb{R}^n \ : \ V(x) \leq \gamma\} \text{ is bounded.} \tag{25}$$

$$\Omega_\gamma \subset \{x \in \mathbb{R}^n \ : \ \nabla V(x) f(x) < 0\} \tag{26}$$

then for all $x \in \Omega_\gamma$, the solution of Equation (21) exists, satisfies $x(t) \in \Omega_\gamma$ for all $t \geq 0$, and $\Omega_\gamma \subset \mathcal{R}$.

A function V, satisfying the conditions in Lemma 1 is a Lyapunov function and Ω_γ provides an estimate of the region of attraction. If $x = 0$ is asymptotically stable, a linearization can be used to compute a Lyapunov function. Let $A := \frac{\partial f}{\partial x}\big|_{x=0}$ be the linearization of the dynamics about the origin and compute $P > 0$ that solves the Lyapunov equation $A^T P + PA = -I$. $V_{LIN}(x) := x^T P x$ is a quadratic Lyapunov function that satisfies the conditions of Lemma 1 for sufficiently small $\gamma > 0$. V_{LIN} can be used to compute a lower bound on β^* by solving two maximizations:

$$\begin{aligned} \gamma^* := & \max \gamma \\ & \text{subject to: } \Omega_\gamma \subset \{x \in \mathbb{R}^n \ : \ \nabla V_{LIN}(x) f(x) < 0\} \end{aligned} \tag{27}$$

$$\begin{aligned} \underline{\beta} := & \max \beta \\ & \text{subject to: } \mathcal{E}_\beta \subset \Omega_{\gamma^*} \end{aligned} \tag{28}$$

The first maximization finds the largest level set Ω_{γ^*} of V_{LIN} such that Lemma 1 can be used to verify $\Omega_{\gamma^*} \subseteq \mathcal{R}$. The second maximization finds the largest ellipsoid $\mathcal{E}_{\underline{\beta}}$ contain within Ω_{γ^*}. The computational algorithm used replaces the set containment constraints with a sufficient condition involving non-negative functions (Tan, 2006). For example, $\mathcal{E}_\beta \subset \Omega_{\gamma^*}$ in Optimization (28) is replaced by

$$\begin{aligned} \underline{\beta} := \max_{\beta,\ s(x)} \ & \beta \\ \text{subject to: } & s(x) \geq 0 \ \forall x \\ & -(\beta - p(x))\, s(x) + (\gamma^* - V_{LIN}(x)) \geq 0 \ \forall x \end{aligned} \tag{29}$$

The function $s(x)$ is a decision variable of the optimization, i.e. it is found as part of the optimization. It is straight-forward to show that the two non-negativity conditions in Optimization (29) are a sufficient condition for the set containment condition in Optimization (28). If $s(x)$ is restricted to be a polynomial then both constraints involve the non-negativity of polynomial functions. A sufficient condition for a generic multi-variate polynomial $h(x)$ to be non-negative is the existence of polynomials $\{g_1, \ldots, g_n\}$ such that $h = g_1^2 + \cdots + g_n^2$. A polynomial which can be decomposed in this way is rather appropriately called a sum-of-squares (SOS). Finally, if we replace the non-negativity conditions in Optimization (29) with SOS constraints, then we arrive at an SOS optimization problem:

$$\begin{aligned} \underline{\beta} := \max & \ \beta \\ \text{subject to: } & s(x) \text{ is SOS} \\ & -(\beta - p(x))s(x) + (\gamma^* - V_{LIN}(x)) \text{ is SOS} \end{aligned} \tag{30}$$

There are connections between SOS polynomials and semidefinite matrices. Moreover, optimization problems involving SOS constraints can be converted and solved as a semidefinite programming optimization. Importantly, there is freely available software to set up and solve these problems (Prajna et al., 2004; Lofberg, 2004; Sturm, 1999; Balas et al., 2009). $\underline{\beta}_{LIN}$ will denote the lower bound obtained from Optimization (30) using the quadratic Lyapunov function obtained from linearized analysis.

Unfortunately, $\underline{\beta}_{LIN}$ is usually orders of magnitude smaller than the upper bound $\bar{\beta}_{MC}$. Several methods to compute better Lyapunov functions exist, including V-s iterations (Jarvis-Wloszek, 2003; Jarvis-Wloszek et al., 2003; Tan and Packard, 2004; Jarvis-Wloszek et al., 2005), bilinear optimization (Tan, 2006), and the use of simulation data (Topcu et al., 2007, 2008). In this paper, the V-s iteration is used. The Lyapunov function $V(x)$ in the iteration is initialized with the linearized Lyapunov function V_{LIN}. The iteration also uses functions $l_1(x) = -\epsilon_1 x^T x$ and $l_2(x) = -\epsilon_2 x^T x$ where ϵ_1 and ϵ_2 are small positive constants on the order of 10^{-6}. The V-s iteration algorithm steps are provided below.

1. $\underline{\gamma}$ **Step**: Hold V fixed and solve for s_2 and γ^*

$$\gamma^* := \max_{s_1 \in \text{SOS}, \gamma} \gamma \quad \text{s.t. } -(\gamma - V)s_2 - \left(\frac{\partial V}{\partial x} f + l_2\right) \in \text{SOS}$$

2. $\underline{\beta}$ **Step**: Hold V, γ^* fixed and solve for s_1 and $\underline{\beta}$

$$\underline{\beta} := \max_{s_1 \in \text{SOS}, \beta} \beta \quad \text{s.t. } -(\beta - p)s_1 + (\gamma^* - V) \in \text{SOS}$$

3. $\underline{V}$ **step**: Hold s_1, s_2, $\underline{\beta}$, γ^* fixed and solve for V satisfying:

$$
\begin{aligned}
&-(\gamma^* - V)s_2 - \left(\frac{\partial V}{\partial x} f + l_2\right) \in \text{SOS} \\
&-(\underline{\beta} - p)s_1 + (\gamma^* - V) \in \text{SOS} \\
&V - l_1 \in \text{SOS}, V(0) = 0
\end{aligned}
$$

4. Repeat as long as the lower bound $\underline{\beta}$ continues to increase.

In the V-s iteration, Lyapunov functions are allowed to be of higher polynomial degree. Increasing the degree of the Lyapunov function will improve the lower bound at the expense of computational complexity. The computational time grows rapidly with the degree of the Lyapunov function. Hence, the results for degree 6 candidates are provided. Software and additional documentation on the V-s iteration is provided at (Balas et al., 2009).

4. Analysis of Generic Transport Models

4.1. Analysis of Short Period Model

In this section the region of attraction for the short period GTM in Equations (19)-(20) is analyzed. Since this model has only two states it is easy to plot and visualize the entire phase plane. The analysis in this section is for illustrative purposes and a more realistic, higher-dimensional example is provided in Section 4.2.

The open-loop short period model can be analytically linearized about the trim condition to obtain a linear short period model: $\dot{\delta x} = A\delta x + B\delta u$ where $\delta x := [\alpha - \alpha_t,\ q - q_t]^T$ and $\delta u := \delta_{elev} - \delta_{elev,t}$. For the trim condition

in Equation (16) the state matrices are given by:

$$A = \begin{bmatrix} \frac{\partial g_1}{\partial \alpha} & \frac{\partial g_1}{\partial q} \\ \frac{\partial g_2}{\partial \alpha} & \frac{\partial g_2}{\partial \alpha} \end{bmatrix} \Bigg|_{(\alpha_t,\ q_t)} = \begin{bmatrix} -3.236 & 0.9227 \\ -45.34 & -4.372 \end{bmatrix} \tag{31}$$

$$B = \begin{bmatrix} \frac{\partial g_1}{\partial \delta_{elev}} \\ \frac{\partial g_2}{\partial \delta_{elev}} \end{bmatrix} \Bigg|_{(\alpha_t,\ q_t,\ \delta_{elev,t})} = \begin{bmatrix} -0.3166 \\ -59.98 \end{bmatrix} \tag{32}$$

The eigenvalues of this linearization are $-3.80 \pm 6.44i$. The trim condition is asymptotically stable since the eigenvalues are in the open left half of the complex plane. Figure 6 shows the phase plane simulation of the linear (dashed) and nonlinear (solid) short period model. Qualitatively, both the linear and nonlinear phase plane have stable spiral characteristics. This qualitative similarity between the linear and nonlinear short period model implies that the nonlinearities are not significant and the results of linear analyses are expected to be valid over a wide range of flight conditions. Moreover, Figure 6 demonstrates that region of attraction for the short period model contains the region of the state space over which the polynomial model is valid. Recall, the region of validity for the polynomial model is mentioned in Section 2.1.

For the purposes of illustration, it is demonstrated that the linearization can fail to detect the effects of significant nonlinearities. Recall that in the GTM model, C_m is based on three look-up tables:

$$C_m(\alpha, \delta_{elev}, \hat{q}) = C_{m,\alpha}(\alpha) + C_{m,\delta_{elev}}(\alpha, \delta_{elev}) + C_{m,\hat{q}}(\alpha, \hat{q}) \tag{33}$$

The look-up table data for pitch damping derivative $C_{m,\hat{q}}$ is provided on a grid of twenty-four values of angle of attack α in $[-0.5236, 0.8727]$ rad ($[-30, 50]$ deg) and fifteen values of normalized pitch rate $\hat{q}$ in $[-7.500 \times 10^{-3}, 7.500 \times$

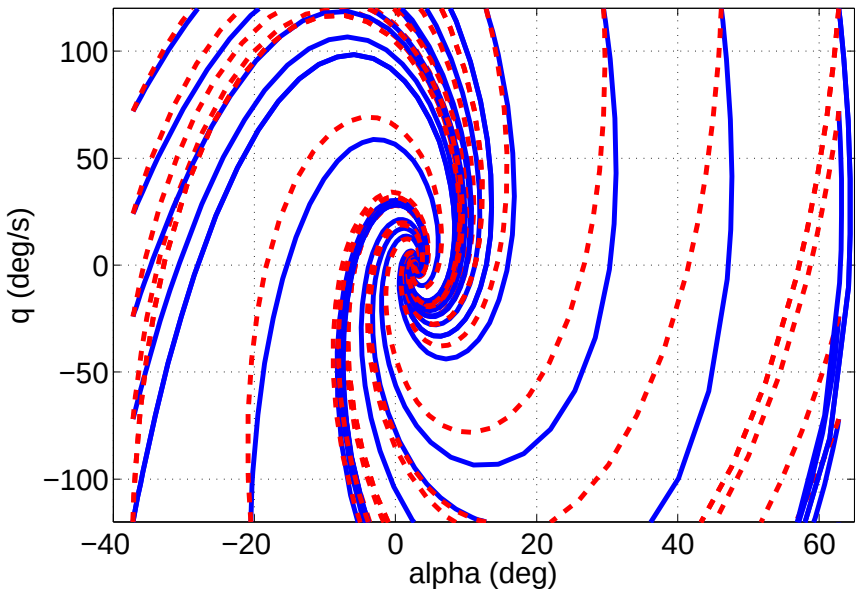

Figure 6: Nonlinear (solid) and linear (dashed) phase plane simulation for polynomial GTM short period model

10^{-3}] (unitless). It is easier to interpret this data in terms of actual rather than normalized pitch rates. The normalized pitch rates in the table grid can be converted at a trim speed V_t to actual pitch rates via the relation $q = \frac{2V_t}{\bar{c}}\hat{q}$. This relation is $q = 322.6\hat{q}$ rad/s (=$1.8484 \times 10^4\hat{q}$ deg/s) at the trim speed $V_t = 45$m/s. Figure 7 shows the raw look-up table data $C_{m,\hat{q}}$ versus q for five different values of α. Each thin solid-dotted line is $C_{m,q}$ vs. q for a specific value of α in the look-up table.

In the polynomial longitudinal model, a linear fit is used to approximate the rate damping look-up table: $C_{m,\hat{q}}(\alpha, \hat{q}) \approx -41.25\hat{q}$. The rate damping is independent of the angle of attack in the approximation. This linear fit can be converted to actual pitch rate (rad/s) at the trim speed $V_t = 45$m/s: $C_{m,\hat{q}} \approx -0.1279q$. Figure 7 also shows the linear fit versus pitch rate in

deg/s (thick solid line). This linear relationship is a typical characteristic of a commercial aircraft like the GTM.

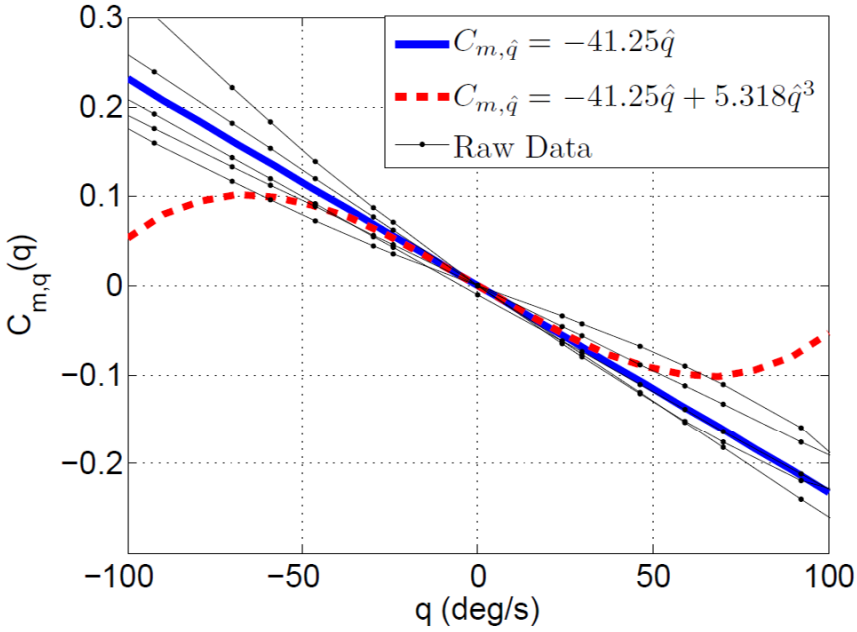

Figure 7: Pitch rate damping vs. pitch rate for raw look-up table data, linear fit, and cubic nonlinearity.

To demonstrate the effects of nonlinearities consider the following cubic pitch rate damping function:

$$C_{m,\hat{q}}(\alpha, \hat{q}) = -41.25\hat{q} + 5.318\hat{q}^3 \tag{34}$$

This function, shown in Figure 7 as a thick dashed curve, results in less damping at higher pitch rates and would lead to a less stable short period model. The inclusion of this cubic term is purely to illustrate the effects of aerodynamic nonlinearities on a simple model. It is not meant to model the behavior of the actual GTM aircraft at high pitch rates. The C_m aerodynamic

coefficient only enters the $\dot{q}$ dynamic equation (Equation (3)). Hence the cubic term modification to $C_{m,\hat{q}}$ only affects the function f_3 in polynomial longitudinal model provided in the Appendix. The updated f_3 based on Equation (34) is given below as $\tilde{f}_3$.

$$\begin{aligned}\tilde{f}_3 = &-6.573\times10^{-9}V^5q^3 + 1.747\times10^{-6}V^4q^3 - 1.548\times10^{-4}V^3q^3 \\ &- 3.569\times10^{-3}V^2\alpha^3 + 4.571\times10^{-3}V^2q^3 + 4.9530\times10^{-5}V^3q \\ &+ 9.596\times10^{-3}V^2\alpha^2 + 2.049\times10^{-2}V^2\alpha\delta_{elev} - 2.431\times10^{-2}V^2\alpha \\ &- 3.063\times10^{-2}V^2\delta_{elev} - 4.388\times10^{-3}V^2q - 2.594\times10^{-7}\delta_{th}^3 \\ &+ 2.461\times10^{-3}V^2 + 1.516\times10^{-4}\delta_{th}^2 + 1.089\times10^{-2}\delta_{th} \\ &+ 1.430\times10^{-1}\end{aligned} \tag{35}$$

The linearization of the updated short period model is unchanged by this modification and is still given by Equations (31) and (32). This statement is verified by noting that $C_{m,\hat{q}}$ only affects the short period linearization through a term of the form:

$$\left.\frac{\partial C_{m,\hat{q}}}{\partial q}\right|_{(\alpha_t,\ q_t)} = \left[-41.25\frac{\bar{c}}{2V} + 15.96\left(\frac{\bar{c}}{2V}q\right)^2\right]\Bigg|_{(\alpha_t,\ q_t)} \tag{36}$$

The second term is due to the cubic nonlinearity but this term is zero since $q_t = 0$ at trim. To summarize, the linearization predicts no change in the aircraft stability when the cubic rate damping term is included.

Figure 8 shows the phase plane for the short period model with this cubic rate damping term. The stable trajectories are in solid while the dashed trajectories grow unbounded. The region of attraction consists of all points that lie on the stable (solid) trajectories. As expected, the cubic term in

$C_{m,\hat{q}}$ decreases the aircraft damping and this reduces the size of the region of attraction.

Figure 8 also shows two ellipsoidal estimates of the region of attraction. These are computed using the V-s iteration as described in the Section 3 but with different shape functions. The solid ellipse is computed with the shape function $p_1(x) = x^T N_1 x$ where $x := [\alpha - \alpha_t,\ q - q_t]$ and $N_1 := diag(0.3491 \text{ rad},\ 0.8727 \text{ rad/s})^{-2} := diag(20 \text{ deg},\ 50 \text{ deg/s})^{-2}$. For this shape function the lower bound on the region of attraction estimate is $\underline{\beta}_1 = 1.76$. This verifies that the ellipse $\mathcal{E}_{\underline{\beta}_1} := \{x \in \mathbb{R}^n \ : \ p_1(x) \leq \underline{\beta}_1\}$ is a subset of the region of attraction. The center of the ellipse is at the trim condition. It has a minor axis length of $20 \text{ deg} \cdot \underline{\beta}_1 = 26.53$ deg along the α axis and a major axis length of $50 \text{ deg/s} \cdot \underline{\beta}_1 = 66.33$ deg/s along the q axis. Note that there is an unstable trajectory that nearly touches the boundary of $\mathcal{E}_{\underline{\beta}_1}$. Thus the ellipsoidal estimate is tight in the sense that any further increase the size of the ellipse will cause it to no longer be a subset of the ROA.

Choosing the shape matrix as $N_2 := diag(0.1745 \text{ rad},\ 0.8727 \text{ rad/s})^{-2} := diag(10 \text{ deg},\ 50 \text{ deg/s})^{-2}$ decreases the shape of the ellipse in the α direction as compared to the q direction. For the shape function $p_2(x) = x^T N_2 x$ the lower bound on the region of attraction estimate is $\underline{\beta}_2 = 5.69$. $\mathcal{E}_{\underline{\beta}_2} := \{x \in \mathbb{R}^n \ : \ p_2(x) \leq \underline{\beta}_2\}$ is shown as the dashed ellipse in Figure 8. This estimate is also tight since it has an unstable trajectory that nearly touches the boundary of the ellipse. This estimate of the region of attraction is significantly larger in q direction than $\mathcal{E}_{\underline{\beta}_1}$ and it is only slightly smaller in the α direction. Ultimately the choice between p_1 and p_2 depends on which direction of the

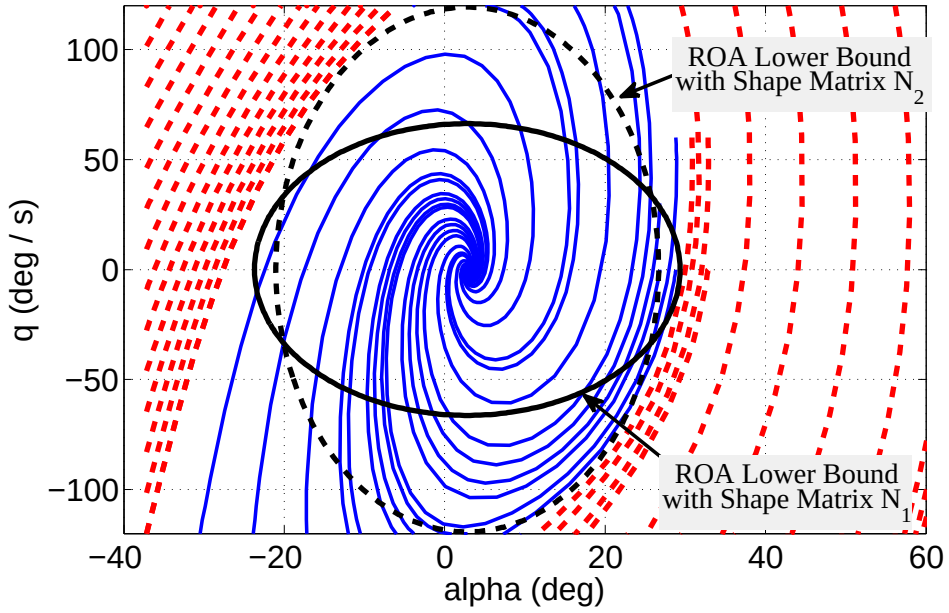

Figure 8: Phase plane simulation for polynomial short period model with cubic $C_{m,\hat{q}}$ with lower bound estimation of ROA for different shape factor; Stable trajectories are denoted by solid and dashed denotes the unstable trajectories

state space is more important to the analyst.

This example demonstrates the benefit of nonlinear region of attraction estimation for flight control analysis. A comparison between Figures 6 and 8 demonstrates that the addition of the cubic pitch rate damping nonlinearity significantly reduced the size of the stability region. However, the short period linearization is unaffected by this nonlinear term and hence linear analyses fail to detect any stability issues. The reduction in the stability region is captured by the nonlinear ROA estimation technique.

This example also graphically demonstrates that impact of the shape function on the region of attraction estimate. In a generic, higher dimen-

sional problem the shape function level sets are ellipsoids. The choice of a shape function would depend on the relative importance and units of the states. The unstable trajectories can also be used to judge the quality of the ellipsoidal ROA lower bounds. For a higher dimensional problems, the phase plane is not easily visualized. The Monte Carlo search described in Section 4.2 is used to compute upper bounds on the optimal ellipsoidal estimate from unstable trajectories. Section 4.2 applies the techniques to computing both lower and upper bounds for the ellipsoidal ROA of the 4-state longitudinal GTM dynamics.

4.2. Analysis of 4-State Longitudinal Model

Phase-plane simulation alone is sufficient to understand the stability regions for 2-state models. However, phase-plane analysis is not applicable when the state dimension is greater than two or three. In this section, the techniques described in Section 3 are used to estimate the stability region of the 4-state longitudinal GTM dynamics with a simple proportional inner-loop control law.

Inner loop pitch rate feedback is typically used to improve the short period damping of the aircraft. The following proportional pitch rate feedback is used to improve the damping of the GTM aircraft:

$$\delta_{elev} = K_q q + \bar{\delta}_{elev} = 0.0698q + \bar{\delta}_{elev} \tag{37}$$

The open loop short period dynamics of the GTM are slightly underdamped. The poles of the short period linearization (Equation 31) have a damping ratio of 0.509. The rate feedback controller increases the damping ratio

to 0.713. Equations (15) and (37) describe the nonlinear dynamics of the closed-loop system with the thrust being held at its trim value.

Region of attraction analysis is performed for the GTM aircraft around the level flight condition at $V = 45$ m/s. The full trim condition is given by Equation (16). The shape function is $p(z) = z^T N z$ where

$$\begin{aligned} N &:= diag(20 \text{ m/s},\ 0.3491 \text{ rad},\ 0.8727 \text{ rad/s},\ 0.3491 \text{ rad})^{-2} \\ &:= diag(20 \text{ m/s},\ 20 \text{ deg},\ 50 \text{ deg/s},\ 20 \text{ deg})^{-2} \end{aligned} \tag{38}$$

The shape function, p, roughly scales each state by the maximum magnitude observed during the flight condition. At straight and level flight, α and θ are expected to have similar deviations. Hence, the maximum deviation for both α and θ are chosen to be of the same magnitude. The velocity is assumed to deviate at most 20 m/s from its trim airspeed of 45 m/s during the flight condition. This range of airspeed ($V \in [25 \text{ m/s},\ 65 \text{ m/s}]$) is outside the range of validity of the model by 5 m/s. Recall, the polynomial model is valid over the range of airspeed from 30 m/s to 60 m/s. The maximum deviation in pitch rate is chosen so that the maximum deviation stays within the range of model validity in the pitch rate direction. The polynomial model is valid for -70 deg/s $\leq q \leq 70$ deg/s.

The polynomial model of the longitudinal dynamics was modified in two ways to make it suitable for the computational algorithms. First the state was redefined as $z := x - x_t := [V - V_t,\ \alpha - \alpha_t,\ q - q_t,\ \theta - \theta_t]^T$ to shift the trim condition to the origin of the state space. Next, all polynomial terms with degree greater than five and/or coefficients less than 10^{-6} were removed from the model. The terms have negligible effect on the model but their

removal greatly reduces the computation time for the lower bounds due to the computation of the V-s iteration growing rapidly with the degree of the polynomial model and the Lyapunov function.

Scaling of the model is another important issue for the numerical stability of the V-s iteration. The magnitude of the coefficients in the fifth order closed-loop polynomial model can vary greatly. For example, the magnitude of the minimum and maximum coefficients in the velocity derivative equation ($\dot{V}$) are 6.860×10^{-6} and 85.38, respectively. Scaling of the state-space of the closed-loop dynamics is used to improve the numerical conditioning. The states are scaled as $z_{scl} = Dz$ where $D = N^2$. In the z_{scl} coordinates the shape function is $p(z_{scl}) = z_{scl}^T z_{scl}$. After scaling the magnitude of the minimum and maximum coefficients in the velocity derivative equation ($\dot{V}$) are 1.197×10^{-4} and 0.520, respectively. The V-s iteration was run on the scaled model and results converted back to unscaled coordinates.

The V-s iteration with a degree six Lyapunov function resulted in a lower bound estimate of $\underline{\beta}_6 = 3.36$. This verifies that the ellipsoid $\mathcal{E}_{\underline{\beta}_6} := \{x \in \mathbb{R}^n : p(x) \leq \underline{\beta}_6\}$ is a subset of the region of attraction. The center of the ellipsoid is at the trim condition. It has a length of 20 deg$\cdot \sqrt{\underline{\beta}_6} = 36.66$ deg along the α axis. The other axis lengths can be computed similarly. The upper bound from Monte Carlo simulation approach is computed to be $\bar{\beta}_{MC} = 3.76$. In other words, Monte Carlo simulation found an unstable trajectory with a point on the ellipsoid $\mathcal{E}_{\underline{\beta}_{MC}}$.

The ellipsoidal bounds on the region of attraction can be visualized by plotting slices of the ellipsoids $\mathcal{E}_{\underline{\beta}_6}$ and $\mathcal{E}_{\underline{\beta}_{MC}}$. Figure 9 shows slices of these ellipsoidal ROA bounds in the α-q plane. The solid ellipse is the slice of

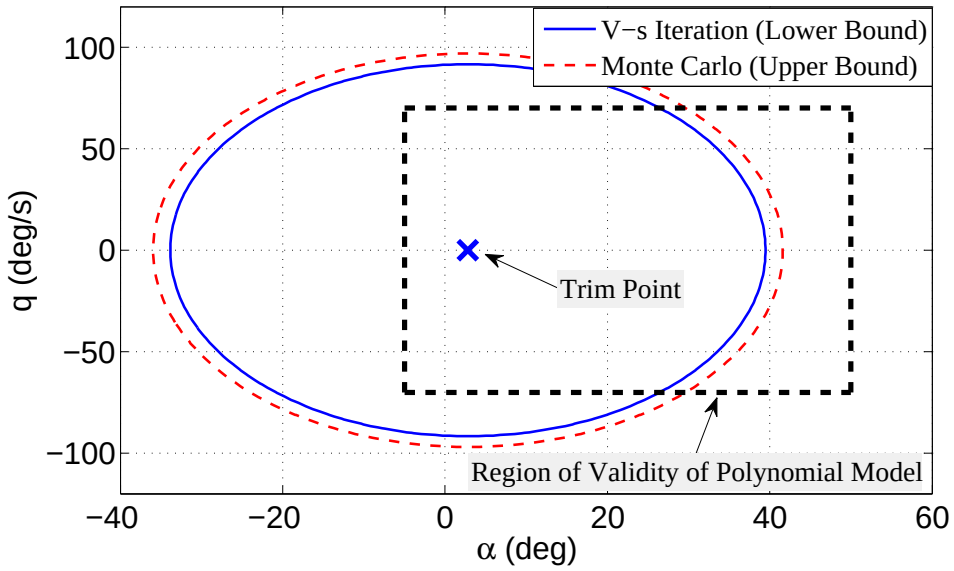

Figure 9: Lower and Upper Bound Estimate of ROA for the GTM longitudinal model; the rectangular region defines the validity region of the model

the $\mathcal{E}_{\underline{\beta}_6}$. Every initial condition within this ellipsoid will return to the trim condition (marked as an 'x'). The dashed ellipse is the slice of $\mathcal{E}_{\underline{\beta}_{MC}}$ in the α-q plane. There is an unstable trajectory that touches $\mathcal{E}_{\underline{\beta}_{MC}}$ although it may not necessarily touch the ellipse in the α-q plane. The Monte Carlo search returned the following initial condition yielding an unstable trajectory.

$$\begin{aligned} x_{0,div} &:= [45.36 \text{ m/s}, \ -0.6231 \text{ rad}, \ 0.3701 \text{ rad/s}, \ 1.1957 \text{ rad}]^T \\ &:= [45.36 \text{ m/s}, \ -35.70 \text{ deg}, \ 21.21 \text{ deg/s}, \ 68.51 \text{ deg}]^T \end{aligned}$$

The dotted rectangular box in Figure 9 shows the region of validity for the model. The region of validity for the polynomial model is explained in Section 2.1. The closeness of the inner and outer ellipsoids implies, for engineering purposes, that the best ROA ellipsoid problem has been solved.

The ellipsoidal bounds in Figure 9 are symmetric about the trim point. This is due to the choice of a shape function p centered at the trim point. The region of interest in the state space is not symmetric about the trim point. For example, the model region of validity is skewed toward positive angles of attack. It is possible to perform the region of attraction analysis with shape functions that are not symmetric about the trim point. However the theoretical and algorithmic details of non-symmetric shape functions have not been fully developed. This will be investigated further in future work.

Both lower ($\underline{\beta}_6$) and upper bounds ($\bar{\beta}_{MC}$) of the ROA ellipsoid provide useful information. The lower bound ellipsoid $\mathcal{E}_{\underline{\beta}_6}$ defines the set of initial conditions for which the control law will bring the aircraft back to its trim point. If the aircraft is perturbed due to a wind gust or other upset condition but remains within this ellipsoid then the control law will recover the aircraft and bring it back to trim. For example, the state $[V,\ \alpha, q,\ \theta]^T$ $= [V_t,\ 30.0 \text{ deg},\ 20.0 \text{ deg/s},\ \theta_t]^T$ is inside $\mathcal{E}_{\underline{\beta}_6}$. If a disturbance pushes the GTM aircraft to this state then the control law will bring the aircraft back to its trim point. The upper bound ellipsoid $\mathcal{E}_{\underline{\beta}_{MC}}$ contains at least one initial condition that will cause the aircraft to diverge from its trim condition. Upset conditions that push the aircraft state to this upper bound ellipsoid could lead to loss of control. In other words, information from these two ellipsoids can be used to draw conclusions about the safe flight envelope. The size of these ellipsoids measure the robustness of the flight control law to disturbances. In summary, the ellipsoids define a metric for the safe flight envelope of the GTM aircraft.

5. Summary

This paper demonstrated the utility of polynomial modeling and region of attraction analysis for aircraft flight control systems. Low degree polynomial models were constructed for the longitudinal and short period dynamics of NASA's GTM aircraft. The nonlinear short period model is of interest since this mode is typically decoupled using a linearization of the longitudinal dynamics. Ellipsoidal region of attraction estimates were computed for both models. These region of attraction estimates provide quantitative information about the nonlinear aircraft dynamics. This is in contrast to linearizations that may be valid only in a small neighborhood of the trim condition.

6. Acknowledgments

This research was partially supported under the NASA Langley NRA contract NNH077ZEA001N entitled "Analytical Validation Tools for Safety Critical Systems" and the NASA Langley NNX08AC65A contract entitled 'Fault Diagnosis, Prognosis and Reliable Flight Envelope Assessment." The technical contract monitors are Dr. Christine Belcastro and Dr. Suresh Joshi respectively.

Appendix A. Longitudinal GTM Model

Appendix A.1. Polynomial Aerodynamic Coefficients

Each aerodynamic coefficient is computed as a sum of three terms which model the aerodynamic effects of the basic airframe, elevator inputs, and

pitch rate. For example, $C_*(\alpha, \delta_{elev}, \hat{q})$ is a sum of three terms each of which is computed from a look-up table:

$$C_*(\alpha, \delta_{elev}, \hat{q}) = C_{*,\alpha}(\alpha) + C_{*,\delta_{elev}}(\alpha, \delta_{elev}) + C_{*,\hat{q}}(\alpha, \hat{q})$$

where * can be replaced by $D,\ L,\ m$ to form the drag force, lift force and pitching moment coefficient, respectively.

The basic airframe coefficients for $C_D,\ C_L,\ C_m$ are:

$$\begin{aligned}
C_{D,\alpha}(\alpha) &= -1.477\alpha^3 + 3.110\alpha^2 - 1.303 \times 10^{-1}\alpha + 3.060 \times 10^{-2} \\
C_{L,\alpha}(\alpha) &= \ \ 2.141\alpha^3 - 6.575\alpha^2 + 5.298\alpha + 5.337 \times 10^{-2} \\
C_{m,\alpha}(\alpha) &= -2.199 \times 10^{-1}\alpha^3 + 5.912 \times 10^{-1}\alpha^2 - 1.498\alpha + 1.516 \times 10^{-1}
\end{aligned}$$

The effects of control surface (elevator) on the aerodynamic coefficients are modeled as:

$$\begin{aligned}
C_{D,\delta_{elev}}(\alpha, \delta_{elev}) = &-5.943 \times 10^{-2}\alpha^2 + 1.435 \times 10^{-1}\alpha\delta_{elev} + 5.967 \times 10^{-2}\delta_{elev}^2 \\
&+ 2.661 \times 10^{-2}\alpha + 2.733 \times 10^{-2}\delta_{elev} - 1.903 \times 10^{-3} \\
C_{L,\delta_{elev}}(\alpha, \delta_{elev}) = &\ \ 4.188 \times 10^{-3}\alpha^2 - 3.438 \times 10^{-1}\alpha\delta_{elev} + 9.293 \times 10^{-2}\delta_{elev}^2 \\
&- 3.497 \times 10^{-2}\alpha + 4.610 \times 10^{-1}\delta_{elev} + 2.543 \times 10^{-3} \\
C_{m,\delta_{elev}}(\alpha, \delta_{elev}) = &\ \ 1.263\alpha\delta_{elev} - 1.887\delta_{elev}
\end{aligned}$$

Finally, the contributions due to the pitch damping are expressed as:

$$\begin{aligned}
C_{D,\hat{q}}(\alpha, \hat{q}) = &-2.197 \times 10^{-2}\alpha^2 + 33.58\alpha\hat{q} - 151.0\hat{q}^2 \\
&- 3.022 \times 10^{-3}\alpha - 9.691 \times 10^{-1}\hat{q} + 2.221 \times 10^{-4} \\
C_{L,\hat{q}}(\alpha, \hat{q}) = &\ \ 2.297 \times 10^{-2}\alpha^2 - 1.359\alpha\hat{q} - 856.7\hat{q}^2 \\
&- 1.673 \times 10^{-2}\alpha + 34.38\hat{q} + 3.703 \times 10^{-3} \\
C_{m,\hat{q}}(\alpha, \hat{q}) = &-41.24\hat{q}
\end{aligned}$$

Appendix A.2. 4-state Polynomial Model

The 4-state polynomial longitudinal model is provided in this subsection. The ordering of the states and inputs are, respectively: $x = [V(\text{m/s}),\ \alpha(\text{rad}),\ q(\text{rad/s}),\ \theta(\text{rad})]$, and $u = [\delta_{elev}(\text{rad}),\ \delta_{th}(\%)]$. The polynomial model is:

$$f(x,u) := [f_1(x,u),\ f_2(x,u),\ f_3(x,u),\ f_4(x,u)]^T$$

$$\begin{aligned}
f_1 = {} & 1.233 \times 10^{-8} V^4 q^2 + 4.853 \times 10^{-9} \alpha^3 \delta_{th}^3 + 3.705 \times 10^{-5} V^3 \alpha q \\
& - 2.184 \times 10^{-6} V^3 q^2 + 2.203 \times 10^{-2} V^2 \alpha^3 - 2.836 \times 10^{-6} \alpha^3 \delta_{th}^2 \\
& + 3.885 \times 10^{-7} \alpha^2 \delta_{th}^3 - 1.069 \times 10^{-6} V^3 q - 4.517 \times 10^{-2} V^2 \alpha^2 \\
& - 2.140 \times 10^{-3} V^2 \alpha \delta_{elev} - 3.282 \times 10^{-3} V^2 \alpha q - 8.901 \times 10^{-4} V^2 \delta_{elev}^2 \\
& + 9.677 \times 10^{-5} V^2 q^2 - 2.037 \times 10^{-4} \alpha^3 \delta_{th} - 2.270 \times 10^{-4} \alpha^2 \delta_{th}^2 \\
& - 2.912 \times 10^{-8} \alpha \delta_{th}^3 + 1.591 \times 10^{-3} V^2 \alpha - 4.077 \times 10^{-4} V^2 \delta_{elev} \\
& + 9.475 \times 10^{-5} V^2 q - 1.637 \alpha^3 - 1.631 \times 10^{-2} \alpha^2 \delta_{th} + 4.903 \alpha^2 \theta \\
& - 4.903 \alpha \theta^2 + 1.702 \times 10^{-5} \alpha \delta_{th}^2 - 7.771 \times 10^{-7} \delta_{th}^3 + 1.634 \theta^3 \\
& - 4.319 \times 10^{-4} V^2 - 2.142 \times 10^{-1} \alpha^2 + 1.222 \times 10^{-3} \alpha \delta_{th} \\
& + 4.541 \times 10^{-4} \delta_{th}^2 + 9.823 \alpha + 3.261 \times 10^{-2} \delta_{th} - 9.807 \theta + 4.284 \times 10^{-1}
\end{aligned}$$

$$
\begin{aligned}
f_2 = & -3.709 \times 10^{-11} V^5 q^2 + 6.869 \times 10^{-11} V \alpha^3 \delta_{th}^3 + 7.957 \times 10^{-10} V^4 \alpha q \\
& + 9.860 \times 10^{-9} V^4 q^2 + 1.694 \times 10^{-5} V^3 \alpha^3 - 4.015 \times 10^{-8} V \alpha^3 \delta_{th}^2 \\
& - 7.722 \times 10^{-12} V \alpha^2 \delta_{th}^3 - 6.086 \times 10^{-9} \alpha^3 \delta_{th}^3 - 2.013 \times 10^{-8} V^4 q \\
& - 5.180 \times 10^{-5} V^3 \alpha^2 - 2.720 \times 10^{-6} V^3 \alpha \delta_{elev} - 1.410 \times 10^{-7} V^3 \alpha q \\
& + 7.352 \times 10^{-7} V^3 \delta_{elev}^2 - 8.736 \times 10^{-7} V^3 q^2 - 1.501 \times 10^{-3} V^2 \alpha^3 \\
& - 2.883 \times 10^{-6} V \alpha^3 \delta_{th} + 4.513 \times 10^{-9} V \alpha^2 \delta_{th}^2 - 4.121 \times 10^{-10} V \alpha \delta_{th}^3 \\
& + 3.557 \times 10^{-6} \alpha^3 \delta_{th}^2 + 6.841 \times 10^{-10} \alpha^2 \delta_{th}^3 + 4.151 \times 10^{-5} V^3 \alpha \\
& + 3.648 \times 10^{-6} V^3 \delta_{elev} + 3.566 \times 10^{-6} V^3 q + 6.246 \times 10^{-6} V^2 \alpha q \\
& + 4.589 \times 10^{-3} V^2 \alpha^2 + 2.410 \times 10^{-74} V^2 \alpha \delta_{elev} - 6.514 \times 10^{-5} V^2 \delta_{elev}^2 \\
& + 2.580 \times 10^{-5} V^2 q^2 - 3.787 \times 10^{-5} V \alpha^3 + 3.241 \times 10^{-7} V \alpha^2 \delta_{th} \\
& + 2.409 \times 10^{-7} V \alpha \delta_{th}^2 + 1.544 \times 10^{-11} V \delta_{th}^3 + 2.554 \times 10^{-4} \alpha^3 \delta_{th} \\
& - 3.998 \times 10^{-7} \alpha^2 \delta_{th}^2 + 3.651 \times 10^{-8} \alpha \delta_{th}^3 + 4.716 \times 10^{-7} V^3 \\
& - 3.677 \times 10^{-3} V^2 \alpha - 3.231 \times 10^{-4} V^2 \delta_{elev} - 1.579 \times 10^{-4} V^2 q \\
& + 2.605 \times 10^{-3} V \alpha^2 + 1.730 \times 10^{-5} V \alpha \delta_{th} - 5.201 \times 10^{-3} V \alpha \theta \\
& - 9.026 \times 10^{-9} V \delta_{th}^2 + 2.601 \times 10^{-3} V \theta^2 + 3.355 \times 10^{-3} \alpha^3 \\
& - 2.872 \times 10^{-5} \alpha^2 \delta_{th} - 2.134 \times 10^{-5} \alpha \delta_{th}^2 - 1.368 \times 10^{-9} \delta_{th}^3 \\
& - 4.178 \times 10^{-5} V^2 + 2.272 \times 10^{-4} V \alpha - 6.483 \times 10^{-7} V \delta_{th} \\
& - 2.308 \times 10^{-1} \alpha^2 - 1.532 \times 10^{-3} \alpha \delta_{th} + 4.608 \times 10^{-1} \alpha \theta \\
& - 2.304 \times 10^{-1} \theta^2 + 7.997 \times 10^{-7} \delta_{th}^2 - 5.210 \times 10^{-3} V \\
& - 2.013 \times 10^{-2} \alpha + 5.744 \times 10^{-5} \delta_{th} + q + 4.616 \times 10^{-1}
\end{aligned}
$$

$$
\begin{aligned}
f_3 = &-6.573 \times 10^{-9} V^5 q^3 + 1.747 \times 10^{-6} V^4 q^3 - 1.548 \times 10^{-4} V^3 q^3 \\
&- 3.569 \times 10^{-3} V^2 \alpha^3 + 4.571 \times 10^{-3} V^2 q^3 + 4.9530 \times 10^{-5} V^3 q \\
&+ 9.596 \times 10^{-3} V^2 \alpha^2 + 2.049 \times 10^{-2} V^2 \alpha \delta_{elev} - 2.431 \times 10^{-2} V^2 \alpha \\
&- 3.063 \times 10^{-2} V^2 \delta_{elev} - 4.388 \times 10^{-3} V^2 q - 2.594 \times 10^{-7} \delta_{th}^3 \\
&+ 2.461 \times 10^{-3} V^2 + 1.516 \times 10^{-4} \delta_{th}^2 + 1.089 \times 10^{-2} \delta_{th} + 1.430 \times 10^{-1}
\end{aligned}
$$

$$
f_4 = q
$$

References

Bailey, R., Hostetler, R., Barnes, K., Belcastro, C. M., Belcastro, C. M., 2005. Experimental validation: Subscale aircraft ground facilities and integrated test capability. In: AIAA Guidance, Navigation, and Control Conference and Exhibit, San Francisco, CA. No. AIAA 2005-6433.

Balas, G., Packard, A., Seiler, P., Topcu, U., 2009. Robustness analysis of nonlinear systems, http://www.cds.caltech.edu/~utopcu/LangleyWorkshop.html.

Chakraborty, A., Seiler, P., Balas, G., 2009. Applications of linear and nonlinear robustness analysis techniques to the F/A-18 flight control laws. In: AIAA Guidance, Navigation, and Control Conference. No. AIAA-2009-5675.

Chiang, H.-D., Thorp, J., 1989. Stability regions of nonlinear dynamical systems: A constructive methodology. IEEE Transactions on Automatic Control 34 (12), 1229–1241.

Cox, D., 2009. The GTM DesignSim v0905.

Davison, E., Kurak, E., 1971. A computational method for determining quadratic Lyapunov functions for nonlinear systems. Automatica 7, 627–636.

Genesio, R., Tartaglia, M., Vicino, A., 1985. On the estimation of asymptotic stability regions: State of the art and new proposals. IEEE Transactions on Automatic Control 30 (8), 747–755.

Gregory, I. M., Cao, C., Xargay, E., Hovakimyan, N., Zou, X., 2009. L_1 adaptive control design for NASA AirSTAR flight test vehicle. In: AIAA Guidance, Navigation, and Control Conference, Chicago, Illinois. No. AIAA 2009-5738.

Hachicho, O., Tibken, B., 2002. Estimating domains of attraction of a class of nonlinear dynamical systems with LMI methods based on the theory of moments. In: Proceedings of the IEEE Conference on Decision and Control. pp. 3150–3155.

Hauser, J., Lai, M., 1992. Estimating quadratic stability domains by nonsmooth optimization. In: Proceedings of the American Control Conference. pp. 571–576.

Heller, M., David, R., Holmberg, J., 2004. Falling leaf motion suppression in the F/A-18 Hornet with revised flight control software. In: AIAA Aerospace Sciences Meeting. No. AIAA-2004-542.

Heller, M., Niewoehner, R., Lawson, P. K., 1999. High angle of attack control law development and testing for the F/A-18E/F Super Hornet. In: AIAA

Guidance, Navigation, and Control Conference. No. AIAA-1999-4051. pp. 541–551.

Heller, M., Niewoehner, R., Lawson, P. K., 2003. On the validation of safety critical aircraft systems, Part I: An overview of analytical & simulation methods. In: AIAA Guidance, Navigation, and Control Conference. No. AIAA 2003-5559.

Jaramillo, P. T., Ralston, J. N., 1996. Simulation of the F/A-18D falling leaf. In: AIAA Atmospheric Flight Mechanics Conference. pp. 756–766.

Jarvis-Wloszek, Z., 2003. Lyapunov based analysis and controller synthesis for polynomial systems using sum-of-squares optimization. Ph.D. thesis, University of California, Berkeley.

Jarvis-Wloszek, Z., Feeley, R., Tan, W., Sun, K., Packard, A., 2003. Some controls applications of sum of squares programming. In: Proceedings of the 42nd IEEE Conference on Decision and Control. Vol. 5. pp. 4676–4681.

Jarvis-Wloszek, Z., Feeley, R., Tan, W., Sun, K., Packard, A., 2005. Positive Polynomials in Control. Vol. 312 of Lecture Notes in Control and Information Sciences. Springer-Verlag, Ch. Controls Applications of Sum of Squares Programming, pp. 3–22.

Jordan, T. L., Bailey, R. M., 2008. NASA Langleys AirSTAR testbed a subscale flight test capability for flight dynamics and control system experiments. In: AIAA Guidance, Navigation and Control Conference and Exhibit, Honolulu, Hawaii. No. AIAA 2008-6660.

Jordan, T. L., Foster, J. V., Bailey, R. M., Belcastro, C. M., 2006. AirSTAR: A UAV platform for flight dynamics and control system testing. In: 25th AIAA Aerodynamic Measurement Technology and Ground Testing Conference, San Francisco, CA. No. AIAA 2006-3307.

Lluch, C. D., 1998. Analysis of the out-of-control falling leaf motion using a rotational axis coordinate system. Master's thesis, Virginia Polytechnic Institue and State University.

Lofberg, J., 2004. Yalmip : A toolbox for modeling and optimization in MATLAB. In: Proceedings of the CACSD Conference. Taipei, Taiwan. URL `http://control.ee.ethz.ch/ joloef/yalmip.php`

Murch, A., 2008. A flight control system architecture for the NASA AirSTAR flight test infrastructure. In: AIAA Guidance, Navigation and Control Conference and Exhibit, Honolulu, Hawaii.

Murch, A., Cox, D. E., Cunningham, K., 2009. Software considerations for subscale flight testing of experimental control laws. In: AIAA Infotech at Aerospace Conference and Exhibit, Washington, United States.

Murch, A., Foster, J., 2007. Recent NASA research on aerodynamic modeling of post-stall and spin dynamics of large transport airplanes. In: 45th AIAA Aerospace Sciences Meeting and Exhibit, Reno, Nevada.

Parrilo, P., 2000. Structured semidefinite programs and semialgebraic geometry methods in robustness and optimization. Ph.D. thesis, California Institute of Technology.

Prajna, S., Papachristodoulou, A., Seiler, P., Parrilo, P. A., 2004. SOSTOOLS: Sum of squares optimization toolbox for MATLAB.

Stevens, B., Lewis, F., 1992. Aircraft Control and Simulaion. John Wiley & Sons.

Sturm, J., 1999. Using SeDuMi 1.02, a MATLAB toolbox for optimization over symmetric cones. Optimization Methods and Software, 625–653.

Tan, W., 2006. Nonlinear control analysis and synthesis using sum-of-squares programming. Ph.D. thesis, University of California, Berkeley.

Tan, W., Packard, A., 2004. Searching for control Lyapunov functions using sums of squares programming. In: 42nd Annual Allerton Conference on Communications, Control and Computing. pp. 210–219.

Tan, W., Topcu, U., Seiler, P., Balas, G., Packard, A., 2008. Simulation-aided reachability and local gain analysis for nonlinear dynamical systems. In: Proceedings of the IEEE Conference on Decision and Control. pp. 4097–4102.

Tibken, B., 2000. Estimation of the domain of attraction for polynomial systems via LMIs. In: Proceedings of the IEEE Conference on Decision and Control. pp. 3860–3864.

Tibken, B., Fan, Y., 2006. Computing the domain of attraction for polynomial systems via BMI optimization methods. In: Proceedings of the American Control Conference. pp. 117–122.

Topcu, U., Packard, A., Seiler, P., 2008. Local stability analysis using simulations and sum-of-squares programming. Automatica 44 (10), 2669–2675.

Topcu, U., Packard, A., Seiler, P., Wheeler, T., 2007. Stability region analysis using simulations and sum-of-squares programming. In: Proceedings of the American Control Conference. pp. 6009–6014.

Vannelli, A., Vidyasagar, M., 1985. Maximal Lyapunov functions and domains of attraction for autonomous nonlinear systems. Automatica 21 (1), 69–80.

Vidyasagar, M., 1993. Nonlinear Systems Analysis, 2nd Edition. Prentice Hall.